

Towards an effective poroelastic model for naturally fractured porous media

Renato Poli¹, Nicolas Espinoza¹, Kamy Sepehrnoori¹

¹The University of Texas at Austin, 200 E. Dean Keeton St., Austin, TX 78712, United States

Abstract

Fractures are present in most oil and gas reservoirs, either naturally or induced by exploitation. While the impact of the fractures on the fluid flow has been extensively investigated, methods for mechanical upscaling into effective models are still limited. Considering the limitations of experimental assessment on the laboratory scale this work proposes the use of a numerical approach to understand the large-scale mechanical response of a fractured rock mass. First, the design and validation of a high-performance poroelastic simulator with conforming fractures are discussed. Then a series of sensitivity analyses assesses the response of the effective linear poroelastic media in presence of a fracture network. A random mesh generator and Monte Carlo simulations the intrinsic uncertainties of the system, both in the continuum and in the fracture domains. The findings indicate that fracture networks cannot be mechanically neglected, especially in scenarios of low effective stress, which is typically the case of shallow reservoirs, increased pore pressure, or fluid injection at low temperatures. It is also clear that the impact on the drained parameters \bar{K} , $\bar{\nu}$ and $\bar{\alpha}$ is strongly correlated to the fracture density, while the undrained parameters \bar{B} and \bar{M} are more sensitive to higher fluid compressibility as the storage added due to fracture opening becomes relevant. Finally, the uncertainty assessment provides rules of thumb for geomechanical model designers looking for effective parameterization on the field scale.

Keywords: Naturally Fractured Reservoirs; Numerical methods; Linear poroelasticity; Biot consolidation; Skempton coefficient.

INTRODUCTION

Significant oil reserves reside in naturally fractured reservoirs (NFRs). In fact, the existence of joints is practically certain in every oil and gas accumulation. Their impact on fluid flow as preferential paths and in the stress-strain mechanical relationship as planes of high deformability is a necessary definition in the early stages of reservoir characterization. In fact, experimental and field data and thorough investigation show undeniably that, in many cases, the performance of such systems relies on the existence of such joints, and not recognizing their existence may lead to the abandonment of economic fields (Aguilera, 1998; Narr et al., 2006; Nelson, 2001; Zareidarmiyan et al., 2021).

If reservoir and geotechnical modelers do not embed the fractures into their models and instead use laboratory results for flow and mechanics as representative samples, the assessment may

1 carry large errors. For that, significant work has been done in the development of effective (or
2 equivalent) models for fractured media to enable consistent numerical characterization of those
3 within reasonable computational effort (Bandis et al., 1983; Barton and Bandis, 1982; Guéguen
4 and Kachanov, 2011; Long et al., 1982; Oda, 1986).

5 The mechanical behavior of the fractures and the fluid interaction with the fracture walls are
6 linked to the understanding of effective stress principles. The concept of effective stress itself is
7 non-unique, as it depends on the context of the analysis (Boutéca and Guéguen, 1999). Several
8 classic experimental and theoretical works have shown that the volumetric strain of the elastic
9 continuum, for example, is linearly proportional to Biot's effective stress, while the rock failure
10 criterion responds better to Terzaghi's effective stress (Brace and Martin, 1968; Cornet and
11 Fairhurst, 1974; Rice, 1977). Hence, we assume a fracture model in which a specific stiffness
12 quantity is associated with Terzaghi's effective stress acting on the fracture surfaces. That is,
13 we assume there is a locally linear relation between the Terzaghi effective stress acting on the
14 fracture wall and the fracture aperture.

15 On a global sense, however, given the complex geometries of the joints and larger ranges of
16 stress and pressure, the fracture mechanical behavior is strongly non-linear (Bandis et al., 1983;
17 Pyrak-Nolte and Morris, 2000). In summary, the more tensile the stress at the fracture surfaces,
18 the larger the fracture aperture, the smaller the contact area, and, consequently, the smaller its
19 specific stiffness. Particularly, one may assume that beyond a given tensile threshold, the
20 fracture-specific stiffness is negligible, whereas, in compressive states, the specific stiffness is
21 likely high enough to be invisible to large-scale analyses. The present paper shows that this
22 effect is indeed relevant for cases where the reservoir is near effective tensile situations, like in
23 abnormally high-pressure scenarios or near injection wells after cold fluid injection.

24 While extensive experimental work has been done in small samples using fractured media,
25 mechanical testing on a larger scale is limited. For that, numerical simulations and analytical
26 approaches may contribute to upscale the laboratory outcomes into the expected behavior of
27 large-sized fractured volumes. In full-scale reservoir geomechanics models, for example, the
28 REV's size can length over 100m, which is impractical for direct experimental investigation.
29 Moreover, the fracture parameters carry significant uncertainty inherently. The numerical
30 upscaling workflow must not deny this fact but rather provide coherent parametric ranges for

1 large-scale analysis.

2 In the linear mechanics literature, a number of analytical models were proposed to derive
3 effective parameters mostly focused on geophysical applications – e.g. (Grechka and Kachanov,
4 2006)The realization that the macroscopic impact of the fractures is proportional to the cubic
5 power of the radius of circular fractures implies that larger fractures dominate the mechanical
6 behavior, while small fractures can be neglected in the analysis.

7 The use of a numerical approach to determine the equivalent elastic compliance tensor for
8 fractured rock masses using commercial simulators has also been reported with success. We
9 remark, however, the less flexibility provided by such tools, which limits the investigation to a
10 few runs (Min and Jing, 2003). (Marinelli et al., 2016) explores a multiscale finite element strategy
11 with cohesive elements to understand the REV as an effective media.

12 (Chen et al., 2020; De Simone et al., 2023) also discuss the effective stress coefficient derivation
13 in saturated fractured media using numerical models. Although insightful, the work lacks a sense
14 of generality and focuses either on a very specific distribution of fractures or on a single
15 parameter. As the fracture network impacts the poroelastic behavior as a whole, it looks more
16 interesting to assess the parameters altogether in a probabilistic sense.

17 We introduce the in-house numerical simulator PMF3D as the main investigation tool. PMF3D
18 uses an automated reproducible framework and is integrated with a High-Performance
19 Computing (HPC) infrastructure for extensive testing. To our knowledge, the proposed workflow
20 uses the most efficient open-source technologies available, exploring parallelism and automated
21 pre- and post-processing.

22 PMF3D is based on the Finite Element Method (FEM) and uses the concept of zero-width
23 cohesive elements to model conforming fractures in a 3D environment, in which the shear and
24 normal cohesive are controlled independently. To the best of our knowledge, the first authors to
25 propose this approach were (Cundall, 1971; Ghaboussi et al., 1973; Goodman et al., 1968).
26 Prior to the implementation of PMF3D, Poli et al. (2021) showed a FEM 3D simulator with
27 fracture propagation and adaptive mesh refinement, which is now partially expanded to 3D. The
28 complexity increase in meshing and computational cost is remarkable, challenging the design
29 towards a high-performance implementation.

1 This paper offers comprehensive sensitivity analyses and expectations of the parameters of an
2 effective linear poroelastic model representing naturally fractured porous media. The objective
3 is to provide robust recommendations and rules of thumb for field-scale geotechnical modeling
4 frameworks. First, we present the mathematical formulation of PMF3D, the numerical
5 discretization, HPC aspects, and validation procedures. Then, conceptual tests show that a
6 single set of orthotropic joints is enough to significantly change the continuum's large-scale
7 response.

8 Towards a more realistic scenario, we present a mesh generator that can control the fracture
9 density of the model, which is an essential parameter in NFRs. Finally, realizing the
10 interdependency and high uncertainty of the fracture network and rock mass models, a Monte
11 Carlo workflow provides guidance to geomechanical designers intending to consider the fracture
12 network when upscaling laboratory-scale results into effective parameters for field-scale
13 reservoir models.

14

Table 1 – Symbols and definitions for linear poroelasticity

Symbol	Description	Unit
Continuum mechanics		
σ_{ij}	Cauchy (total) stress tensor (positive for tension, negative for compression)	Pa
p	Pore pressure (positive for compression)	Pa
u_{ij}	Displacement tensor	m
C_{ijkl}	Poroelastic stiffness fourth-order tensor	Pa
$\varepsilon_{ij} = \frac{1}{2}(u_{i,j} + u_{j,i})$	Strain tensor.	–
$\epsilon = \frac{\delta V}{V} = \varepsilon_{kk}$	Volumetric strain	–
$\sigma'_{ij} = \sigma_{ij} + \delta_{ij} \alpha p$	Biot effective stress (positive for tension, negative for compression)	Pa
$\sigma''_{ij} = \sigma_{ij} + \delta_{ij} p$	Terzaghi effective stress (positive for tension, negative for compression)	Pa
$\sigma = K\epsilon - \alpha p$	Isotropic applied stress field (positive for tension, negative for compression)	Pa
Drained parameters		
G	Isotropic shear modulus	Pa
$\nu = -\frac{\delta \varepsilon_{\perp}}{\delta \varepsilon_x}$	Isotropic Poisson ratio	–
$E = 2G(1 + \nu)$	Drained Young modulus	Pa
$K = \frac{\delta \sigma}{\delta \epsilon} \Big _{\delta p=0} = \frac{E}{3(1 - 2\nu)}$	Drained bulk modulus.	Pa
$\bar{\nu}, \bar{K}, \bar{\alpha}$	Effective Poisson, Bulk modulus and Biot parameters.	–
$\alpha = \frac{\delta \zeta}{\delta \epsilon} \Big _{\delta p=0}$	Biot coefficient	–
V	Bulk volume of the REV	m ³
REV	Representative elementary volume	
$\zeta = \frac{\delta V_p - \delta V_f}{V} = \alpha \epsilon + p S_{\epsilon}$	Fluid content of the REV (positive for fluid added)	–
$\delta V_p = V_p^1 - V_p^0$	Variation of volume of voids from configuration 0 to configuration 1	m ³
$\delta V_f = V_f^1 - V_f^0$	Variation of volume of solids from configuration 0 to configuration 1	m ³
Undrained parameters		
$B = -\frac{\delta p}{\delta \sigma} \Big _{\delta \zeta=0} = \frac{\delta \epsilon}{\delta \zeta} \Big _{\delta \sigma=0}$	Skempton coefficient	–
\bar{B}	Effective Skempton coefficient.	–
$M = \frac{\delta p}{\delta \zeta} \Big _{\delta \epsilon=0} = \frac{BK}{\alpha(1 - \alpha B)}$	Biot modulus	Pa
$S_{\epsilon} = \frac{1}{M}$	Fluid storage coefficient in constant strain	Pa ⁻¹
$c = \frac{\hat{\kappa}}{\hat{S}}$	Consolidation coefficient.	m ² s ⁻¹
$S = S_{\epsilon} + \frac{\alpha^2(1 - 2\nu)}{2G(1 - \nu)}$	Storage coefficient.	Pa ⁻¹
$p_0 = -\frac{\eta \sigma_z}{G \hat{S}}$	Pressure of the system under undrained conditions.	Pa
$\eta = \frac{\alpha(1 - 2\nu)}{2(1 - \nu)}$	Poroelastic stress coefficient.	–

Fracture mechanics		
\tilde{E}_{η}''	Terzaghi effective specific stiffness normal to the fracture surface	Pa m^{-1}
$\tilde{E}_{\xi}, \tilde{E}_t$	Total specific stiffness tangential to the fracture surface, expressed in the fracture local coordinate system	Pa m^{-1}
\tilde{t}_i	Total cohesive traction in the fracture surface expressed in the fracture local coordinate system (η, ξ, t)	N
$\tilde{t}_{\eta}'' = \tilde{t}_{\eta} + p$	Terzaghi effective cohesive traction normal to the fracture surface.	N
t_i	Total cohesive traction in the fracture surface expressed in the global coordinate system (x, y, z)	N
$t_i' = t_i + \alpha p n_i$	Biot effective cohesive traction in the fracture surface expressed in the global coordinate system (x, y, z)	N
$t_i'' = t_i + p n_i$	Terzaghi effective cohesive traction in the fracture surface expressed in the global coordinate system (x, y, z)	N
$w_{\eta} = \llbracket u_k \rrbracket n_k$	The aperture normal to the fracture surface.	m
Fluid flow		
κ	Rock intrinsic permeability	m^2
μ	Fluid viscosity	$\text{Pa} \cdot \text{s}$
$\hat{\kappa} = \frac{\kappa}{\mu}$	Mobility coefficient.	$\text{m}^2 \text{Pa}^{-1} \text{s}^{-1}$
$\kappa^f, \hat{\kappa}^f$	The intrinsic permeability and the ration between permeability and viscosity in the fracture domain	m^2
$\hat{K}_{ij} = \frac{\hat{\kappa}_{ij}}{\mu}$	Mobility coefficient tensor.	$\text{m}^2 \text{Pa}^{-1} \text{s}^{-1}$

1

2

Table 2 – Mathematical conventions

Symbol	Description
$\dot{\blacksquare} = \frac{d \blacksquare}{dt}$	Time derivative
$\delta_{ij} = \begin{cases} 1, & i = j \\ 0, & i \neq j \end{cases}$	Dirak delta
$\{n_i, s_i, t_i\}$	Outwards unitary normal and tangential vectors to a 2D surface, expressed in the global (x, y, z) coordinate system
$R_{ij} = [n_i \quad s_i \quad t_i]$	Matrix to rotate vectors and matrices from local (η, ξ, t) to global (x, y, z) coordinate system, and vice-versa.
$u_k v_k = \sum_k u_k v_k$	In indicial notation, repeated indices represent summation and the summation sign is ommitted.
$u_{i,j} = \frac{du_i}{dx_j}$	Partial derivative in indicial notation, where x_i refers to the axes of the coordinate system.
$u_{k,k} = \nabla \cdot u_i$	Divergence operator applied to the vector u_i .
$p_{,i} = \nabla p$	Gradient operator over a scalar p
$\tilde{u}_i = R_{ki} u_k$	Rotation of vector u_i from global to local coordinate system
$E_{ij} = R_{ki} R_{lj} \tilde{E}_{kl}$	Rotation of tensor \tilde{E}_{ij} from local to global coordinate system
$\llbracket u_i \rrbracket = u_i^+ + u_i^-$	Jump operator applied to the displacement vector u_i
u_i^+, u_i^-	Displacement vector across a discontinuity. The superscript + and – identify the opposing sides of the discontionuity.

3

4

1 FORMULATION

2 This section presents the mathematical formulation for the in-house simulator PMF3D in the so-called strong form. The numerical domain is split into a *continuum domain* representing the fluid flow and mechanical deformation of the intact rock and a fracture domain representing the fluid flow and mechanical equilibrium along rock joints.

6 The continuum constitutive law follows the linear poroelasticity as originally proposed by (Biot, 1941) and comprehensively described in textbooks (Cheng, 2016; Wang, 2000). In the fracture domain, the models for mechanical equilibrium and flow continuity in the fracture domain follow principles of local linearity, as proposed initially by (Cundall, 1971; Goodman et al., 1968).

10 Symbols and fundamental formulations of poroelasticity used in this work are presented in Table 1. This work uses indicial notation for vectors and tensors to favor implementing low-level computer routines.

13 Continuum domain: linear poroelasticity and flow continuity

14 In linear poroelasticity, the effective stress tensor is linearly related to the strain tensor by

$$\sigma'_{ij} = C_{ijkl} \varepsilon_{kl} , \quad (1)$$

16 where C_{ijkl} is the stiffness tensor, which, for linear elastic media, is

$$C_{ijkl} = \frac{2G\nu}{1-2\nu} \delta_{ij} \delta_{kl} + G(\delta_{ik} \delta_{jl} + \delta_{il} \delta_{jk}) . \quad (2)$$

18 The mechanical equilibrium condition for a REV is given by the divergence-free condition of the Cauchy total stress tensor, that is

$$\sigma_{ij,j} = 0 . \quad (3)$$

21 Using relations in Table 1 and observing the symmetric properties of C_{ijkl} it is clear that

$$C_{ijkl} u_{k,lj} - \alpha p_{,i} = 0 , \quad (4)$$

23 which are said to be the constitutive partial differential equations for the mechanical equilibrium of the continuum.

25 To achieve flow continuity, the rate of increment of fluid content must balance the fluid entering minus leaving the continuum REV, that is

$$\dot{\zeta} + q_{k,k} = 0 \quad . \quad (5)$$

Darcy's law states that the fluid flow through the REV is given by the inner product of the hydraulic conductivity tensor and the gradient of the por pressure in excess:

$$q_i = -\hat{K}_{ik} p_{,k} \quad . \quad (6)$$

Considering horizontal single-phase isotropic flow, the flow equilibrium constitutive partial differential equation becomes

$$\alpha \varepsilon_{kk} + S_\epsilon \dot{p} - \hat{K} p_{,kk} = 0 \quad (7)$$

Fracture domain: flow continuity and mechanical equilibrium

To achieve flow continuity in the fracture domain, the rate of increment of the normal aperture w_η must balance the fluid entering minus the leaving the fracture REV, that is

$$\dot{\zeta}_f + q_{k,k} = 0 \quad \text{on } \Omega_f. \quad (8)$$

This work considers the system to be in a steady state so that, in the fracture domain, the fluid flow is in equilibrium with the surrounding continuum, and the flow across the fracture surface is negligible.

Inside the fracture domain, in the direction η normal to the fracture surface, the fluid is free to flow, and no pressure gradient is expected. Along the fracture, on the other hand, the fluid flow equations can be reduced in dimension and characterized by tangential transmissibility relating fluid flow to the pressure gradient. This formulation is normally referred to as the *cubic law* (Lomize, 1951; Witherspoon et al., 1980). Hence, the fluid flow along the fracture becomes

$$q_k = \hat{K}^f p_{,k} \quad \text{on } \Gamma_f. \quad (9)$$

Note that, for the present study, \hat{K}^f is assumed constant and high enough for steady-state observations.

The fluid content ζ_f inside the fracture can be approximated by the normal aperture w_η , also reducing the dimensionality of the domain, and the flow inside the fracture is fully described by

$$[[\dot{u}_k]] n_k + \hat{K}^f p_{,kk} = 0 \quad \text{on } \Gamma_f \quad (10)$$

The mechanical equilibrium in the fracture domain is controlled by cohesive forces described in

the local coordinate system $\{\eta, \xi, \iota\}$. The parameters $\tilde{E}_\eta, \tilde{E}_\xi, \tilde{E}_\iota$ are the specific stiffness in the normal and tangential directions to control the fracture mechanics. For the present work, $\tilde{E}_\xi = \tilde{E}_\iota$ in all cases. Hence, the fracture Terzaghi effective cohesive traction in the local coordinate system is

$$\tilde{t}_k'' = \tilde{E}_{kl} \tilde{w}_l \quad i, k \in \{\eta, \xi, \iota\} \quad (11)$$

where

$$\tilde{E}_{ij} = \begin{bmatrix} \tilde{E}_\eta & 0 & 0 \\ 0 & \tilde{E}_\xi & 0 \\ 0 & 0 & \tilde{E}_\iota \end{bmatrix} \quad i, j \in \{\eta, \xi, \iota\} . \quad (12)$$

Note that a zero stiffness represents a cohesion-free fracture, meaning that the fracture surfaces do not interact. However, the fluid pressure inside the fracture still acts as a total normal stress with $\tilde{t}_k'' = 0$ or, equivalently, $t_i = -p n_i$.

The rotation tensor R_{ij} must be applied to rotate (11) into the global coordinate system. As the aperture in the local coordinate system is

$$\tilde{w}_l = R_{lj} w_j = R_{lj} \llbracket u_j \rrbracket \quad \text{on } \Gamma_f , \quad (13)$$

the Terzaghi effective cohesive traction in the global coordinate system is

$$\tilde{t}_k'' = R_{ki} t_i'' , \quad (14)$$

and observing the orthogonal nature of the rotation matrix,

$$R_{ij}^{-1} = R_{ij}^T = R_{ji} , \quad (15)$$

the traction acting on the fracture surface in global coordinates is

$$t_i'' = R_{ki} R_{lj} \tilde{E}_{kl} \llbracket u_j \rrbracket . \quad (16)$$

Lastly, the Biot effective cohesive traction on the face of the fracture as

$$t_i' = t_i'' + (\alpha - 1)p n_i . \quad (17)$$

The final expression for the t_i' is

$$t_i' = R_{ki} R_{lj} \tilde{E}_{kl} \llbracket u_j \rrbracket + (\alpha - 1)p n_i \quad \text{on } \Gamma_f \quad (18)$$

1 NUMERICAL SOLUTION

2 The space discretization follows the Finite Element Method (FEM) as described by (Hughes,
3 2000). Numerical stability is ensured by LBB stability condition using second-order basis
4 functions for displacement variables and first-order shape functions for pressure (Murad and
5 Loula, 1994). The fracture model uses elements of reduced dimension; that is, the dimension
6 normal to the fracture surface is analytically reduced as flow and traction boundary conditions
7 for the continuum and only the tangential flow is solved numerically as 2D surface elements.
8 Time marching follows second-order implicit Crank-Nicholson time-stepping, with a proven gain
9 in performance and accuracy compared to first-order implicit schemes during validation tests.

10 Space discretization using the Finite Element Method

11 This section presents the formal statement of the problem in a Finite Element environment. Table
12 3 summarizes definitions for the development that follows. Equations (4, 7, 10, 18) comprise the
13 strong form (S) of the problem, rewritten below for clarity:

14	(S) Find $u_i \in \mathcal{U}_i$ and $p \in \mathcal{P}$, such that:	
15	Continuum mechanics:	$C_{ijkl} u_{k,lj} - \alpha p_{,i} = 0$ on Ω
16	Continuum flow and mass balance:	$\alpha \varepsilon_{kk} + S_\epsilon \dot{p} - \hat{\kappa} p_{,kk} = 0$ on Ω
17	Fracture mechanics:	$[[\dot{u}_k]] n_k + \hat{\kappa}^f p_{,kk} = 0$ on Γ_f
18	Fracture flow and mass balance:	$t'_i = R_{ki} R_{lj} \tilde{E}_{kl} [[u_j]] + (\alpha - 1) p n_i$ on Γ_f
19	Boundary conditions:	$u_i = \tilde{u}_i$ and $p = \tilde{p}$ on $\Gamma \setminus \Gamma_f$ (19)

20 For the coupling between the fracture and continuum domains, it is convenient to write the weak
21 form of equation (10) and perform the integral by parts:

$$22 \quad (\psi, [[\dot{u}_k]] n_k)_{\Gamma_f} - \hat{\kappa}^f (\psi, p_{,k})_{\Gamma_f} + (\psi, q_\eta)_{\Gamma_f} = 0, \quad \forall \psi \in \mathcal{Q}. \quad (20)$$

23 Ignoring the fluid flow normal to the fracture surface (second term), the fluid exchange with the
24 continuum becomes

$$25 \quad (\psi, q_\eta)_{\Gamma_f} = \hat{\kappa}^f (\psi, p_{,k})_{\Gamma_f} - (\psi, [[\dot{u}_k]] n_k)_{\Gamma_f}, \quad \forall \psi \in \mathcal{Q}, \quad (21)$$

26 that is the coupling term.

1 Splitting the continuum boundary into a fracture boundary Γ_f and a non-fracture boundary $\Gamma \setminus \Gamma_f$,
 2 the weak form (W_c) that derives from the continuum domain equations (4, 7) is

3 (W_c) Find $u_i \in \mathcal{U}_i$ and $p \in \mathcal{P}$, such that $\forall \varphi_i \in \mathcal{V}_i$ and $\forall \psi \in \mathcal{Q}$:

4 Continuum mechanics:

$$5 \quad a(\varphi_i, u_i)_\Omega + (\varphi_i, p_i)_\Omega - (\varphi_i, t'_i)_{\Gamma_f} - (\varphi_i, t'_i)_{\Gamma \setminus \Gamma_f} +$$

6 Continuum flow and mass balance:

$$7 \quad (\psi, \alpha \dot{u}_{k,k} + S_\epsilon \dot{p})_\Omega - (\psi, \hat{\kappa} p_k)_\Omega - (\psi, q_\eta)_{\Gamma_f} - (\psi, q_n)_{\Gamma \setminus \Gamma_f}$$

$$8 \quad = 0$$

9 where

$$10 \quad a(\varphi_i, u_i) = \int_\Omega C_{ijkl} \varphi_{i,j} u_{i,l} d\Omega . \quad (22)$$

11 Replacing t'_i and q_η at the fracture boundary Γ_f , the continuum domain is coupled to the fracture
 12 domain in a single weak form (W):

13 (W) Find $u_i \in \mathcal{U}_i$ and $p \in \mathcal{P}$, such that $\forall \varphi_i \in \mathcal{V}_i$ and $\forall \psi \in \mathcal{Q}$

14 Continuum mechanics:

$$15 \quad a(\varphi_i, u_i)_\Omega + (\varphi_i, p_i)_\Omega - (\varphi_i, t'_i)_{\Gamma \setminus \Gamma_f}$$

16 Continuum flow and mass balance:

$$17 \quad + (\psi, \alpha \dot{u}_{k,k})_\Omega + (\psi, S_\epsilon \dot{p})_\Omega - (\psi, \hat{\kappa} p_k)_\Omega - (\psi, q_n)_{\Gamma \setminus \Gamma_f}$$

18 Fracture mechanics:

$$19 \quad -(\varphi_i, R_{ki} R_{lj} \tilde{E}_{kl} \llbracket u_j \rrbracket)_{\Gamma_f} - (\varphi_i, (\alpha - 1)p n_i)_{\Gamma_f}$$

20 Fracture flow and mass balance:

$$21 \quad -\hat{\kappa}^f (\psi, p_k)_{\Gamma_f} + \hat{\kappa}^f (\psi, p_k n_k)_{\Gamma_f} - (\psi, \llbracket \dot{u}_k \rrbracket n_k)_{\Gamma_f}$$

$$22 \quad = 0 \quad (23)$$

1 and the Galerkin form (G) becomes

2 (G) Find $u_i^h = v_i^h + \check{u}_i^h \in \mathcal{U}_i^h \subset \mathcal{U}_i$ and $p^h = \varphi^h + \check{p}^h \in \mathcal{P}^h \subset \mathcal{P}$, such that

$$3 \quad \forall \varphi_i^h \in \mathcal{V}_i^h \subset \mathcal{V}_i \text{ and } \forall \psi^h \in \mathcal{Q}^h \subset \mathcal{Q}$$

4 Continuum mechanics:

$$5 \quad a(\varphi_i^h, [v_i^h + \check{u}_i^h])_{\Omega} + (\varphi_i^h, [\varphi_{,i}^h + \check{p}_{,i}^h])_{\Omega} - (\varphi_i, t_i'^h)_{\Gamma \setminus \Gamma_f}$$

6 Continuum flow and mass balance:

$$7 \quad +(\psi^h, \alpha [\dot{v}_{k,k}^h + \check{u}_{k,k}^h] + S_{\epsilon} [\dot{\varphi}^h + \check{p}^h])_{\Omega} - (\psi_{,k}, \hat{\kappa} [\varphi_{,k}^h + \check{p}_{,k}^h])_{\Omega} - (\psi, q_n)_{\Gamma \setminus \Gamma_f}$$

8 Fracture mechanics:

$$9 \quad -(\varphi_i^h, R_{ki} R_{lj} \tilde{E}_{kl} \llbracket v_j^h + \check{u}_j^h \rrbracket)_{\Gamma_f} - (\varphi_i^h, (\alpha - 1)[\varphi^h + \check{p}^h] n_i)_{\Gamma_f}$$

10 Fracture flow and mass balance:

$$11 \quad -(\psi_{,k}^h, \hat{\kappa}^f [\varphi_{,k}^h + \check{p}_{,k}^h])_{\Gamma_f} + (\psi^h, \hat{\kappa}^f n_k [\varphi_{,k}^h + \check{p}_{,k}^h])_{\Gamma_f} - (\psi^h, \llbracket \dot{v}_k + \check{u}_k \rrbracket n_k)_{\Gamma_f}$$

$$12 \quad = 0 . \quad (24)$$

13 The system is now split into elements and nodes to be evaluated in a linear system of equations.

14 The iterators $\beta, \gamma \in \{1 \dots N\}$ are now introduced to represent the mesh nodes and associated
15 degrees of freedom $\{v_i^{\gamma}, q^{\gamma}\}$, which are the unknowns of the global linear equation system

$$16 \quad \mathbf{K}^{\beta\gamma} \begin{bmatrix} v_i^{\gamma} \\ q^{\gamma} \end{bmatrix} = \mathbf{F}^{\beta} . \quad (25)$$

17 From equation (24), v_i^h and q^h are approximated as the linear combinations of the shape
18 functions φ^{γ} and ψ^{γ} to obtain the coefficient matrix $\mathbf{K}^{\beta\gamma}$ and right-hand-side vector \mathbf{F}^{β} . That is

$$19 \quad v_i^h = v_i^{\gamma} \varphi^{\gamma} \quad \text{and} \quad q^h = q^{\gamma} \psi^{\gamma} . \quad (26)$$

20 The time derivatives $\{\dot{v}_i^h, \dot{p}^h\}$ in equation (24) are linearly expanded as

$$21 \quad \dot{\blacksquare} = \frac{1}{\Delta t} (\blacksquare^{t+1} - \blacksquare^t) , \quad (27)$$

22 where the term \blacksquare^t is known from the previous iteration or from initial conditions, and the term
23 \blacksquare^{t+1} is the unknown.

24 The second-order implicit Crank-Nicholson scheme approximates the terms $\{v_i^h, p^h\}$, such that

$$25 \quad \blacksquare = \frac{1}{2} (\blacksquare^{t+1} + \blacksquare^t) , \quad (28)$$

Where the coefficient of the unknowns \mathbf{K}^{t+1} comprise the $\mathbf{K}^{\beta\gamma}$ tangent matrix, while the coefficients of the \mathbf{K}^t can be fully evaluated and summed into the right-hand side vector \mathbf{F}^β . In our experience, the second-order time approximation is accurate and efficient, requiring fewer timesteps than the first-order implicit or explicit system.

Finally, the system parameters are assumed locally constant and leave the integrals. The expression for $\mathbf{K}^{\beta\gamma}$ and \mathbf{F}^β and the full matrix equivalent statement (M) are long and verbose and are not listed for the benefit of clarity. They are derived from substituting equations (25) to (28) in the statement below.

(M) Find $\mathbf{v}_i^\gamma, \mathbf{q}^\gamma \in \mathbb{R}^N$ such that:

Continuum mechanics:

$$\begin{aligned} & \mathbf{v}_i^\gamma a(\varphi_i^\beta, \varphi_i^\gamma) + \mathbf{p}^\gamma(\varphi_i^\beta, \varphi_i^\gamma) - (\varphi_i^\beta, \mathbf{t}_i')_{\Gamma \setminus \Gamma_f} \\ & + \check{\mathbf{u}}_i^\gamma a(\varphi_i^\beta, \varphi^\gamma) + \check{\mathbf{p}}^\gamma(\varphi_i^\beta, \psi_{,i}^\gamma) \end{aligned}$$

Continuum flow and mass balance:

$$\begin{aligned} & + \alpha \dot{\mathbf{v}}^\gamma(\psi^\beta, \psi_{,k}^\gamma) + S_\epsilon \mathbf{p}^\gamma(\psi^\beta, \psi^\gamma) - \hat{\kappa} \mathbf{p}_{,k}^\gamma(\psi_{,k}^\beta, \psi_{,k}^\gamma) - (\psi^\beta, \mathbf{q}_n)_{\Gamma \setminus \Gamma_f} \\ & + \alpha \check{\mathbf{u}}_k^\gamma(\psi^\beta, \varphi_{,k}^\gamma) + S_\epsilon \check{\mathbf{p}}^\gamma(\psi^\beta, \psi^\gamma) - \hat{\kappa} \check{\mathbf{p}}^\gamma(\psi_{,k}^\beta, \psi_{,k}^\gamma) \end{aligned}$$

Fracture mechanics:

$$\begin{aligned} & - \llbracket \mathbf{v}_j^\gamma \rrbracket R_{ki} R_{lj} \tilde{E}_{kl} (\varphi_i^\beta, \varphi^\gamma)_{\Gamma_f} - \mathbf{p}^\gamma(\alpha - 1) n_i (\varphi_i^\beta, \psi^\gamma)_{\Gamma_f} \\ & - \llbracket \check{\mathbf{u}}_j^\gamma \rrbracket R_{ki} R_{lj} \tilde{E}_{kl} (\varphi_i^\beta, \varphi^\gamma)_{\Gamma_f} - \check{\mathbf{p}}^\gamma(\alpha - 1) n_i (\varphi_i^\beta, \psi^\gamma)_{\Gamma_f} \end{aligned}$$

Fracture flow and mass balance:

$$\begin{aligned} & - \hat{\kappa}^f \mathbf{q}^\gamma(\psi_{,k}^\beta, \varphi_{,k}^\gamma) + \hat{\kappa}^f \mathbf{p}^\gamma n_k (\psi^\beta, \varphi_{,k}^\gamma) - \llbracket \dot{\mathbf{v}}_k^\gamma \rrbracket n_k (\psi^\beta, \varphi^\gamma) \\ & - \hat{\kappa}^f \check{\mathbf{p}}^\gamma(\psi_{,k}^\beta, \psi_{,k}^\gamma) + \hat{\kappa}^f \check{\mathbf{p}}^\gamma n_k (\psi^\beta, \psi_{,k}^\gamma) - \llbracket \check{\mathbf{u}}_k^\gamma \rrbracket n_k (\psi^\beta, \varphi^\gamma) \\ & = 0 . \end{aligned}$$

(29)

Table 3 – Symbols and relevant definitions for the Finite Element Method framework

Symbol	Description
$\mathcal{U}_i = \{u_i \mid u_i \in H^1, u_i(\Gamma) = \check{u}_i\}$	Collection of the trial solutions for displacement.
$\mathcal{P} = \{p \mid p \in H^1, p(\Gamma) = \check{p}\}$	Collection of the trial solutions for pressure.
$\mathcal{V}_i = \{\varphi_i \mid \varphi_i \in H^1, \varphi_i(\Gamma) = 0\}$	Collection of the test solutions for displacement.
$\mathcal{Q} = \{\psi \mid \psi \in H^1, \psi(\Gamma) = 0\}$	Collection of the test solutions for pressure.
$\mathcal{U}_i^h, \mathcal{P}^h, \mathcal{V}_i^h, \mathcal{Q}^h$	The discrete counterparts of the function spaces $\mathcal{U}_i, \mathcal{P}, \mathcal{V}_i, \mathcal{Q}$
$v_i^h = v_i^\gamma \varphi^\gamma$	Linear combination of shape functions φ^γ to approximate v_i^h .
$p^h = p^\gamma \psi^\gamma$	Linear combination of shape functions ψ^γ to approximate p^h .
$\check{u}_i^h, \check{p}^h$	Heterogeneous (non-zero) Dirichlet (natural) constraints for u_i^h and p^h .
$\llbracket u_j^h \rrbracket = (u_j^{\gamma+} - u_j^{\gamma-}) \varphi^\gamma$	Approximation of the jump operator across a discontinuity. The positive (+) superscript represents the displacement on the positive face of the fracture and the negative (−) represent the displacement in the negative face of the fracture.
N	Number of nodes in the mesh.
$(u, v)_\Omega = \int_\Omega uv \, d\Omega \quad u, v: \Omega \rightarrow \mathbb{R}$	L_2 inner product of functions u and v over the continuum domain Ω .
$(u, v)_{\Gamma_f} = \int_{\Gamma_f} uv \, d\Gamma \quad u, v: \Gamma_f \rightarrow \mathbb{R}$	L_2 inner product of functions u and v over the fracture domain Γ_f .
$\ u\ = (u, u)^{\frac{1}{2}} \quad u: \Omega \rightarrow \mathbb{R}$	L_2 norm of u over the domain Ω .
$L_2 = \{u \mid \ u\ < \infty\}$	The Hilbert space L_2 is defined as the collection of square integrable functions $u: \Omega \rightarrow \mathbb{R}$ (finite L_2 norm).
$(u, v)_s = \int_\Omega (u_i v_i + u_{i,k} v_{i,k} + \dots) d\Omega \quad u, v: \Omega \rightarrow \mathbb{R}$	H_s inner product of functions u and v over the domain Ω .
$\ u\ _s = (u, u)_s^{\frac{1}{2}}$	H_s norm of u over domain Ω .
$H_s = \{u \mid \ u\ _s < \infty\}$	The s^{th} Sobolev space H_s is defined as the collection of functions u with finite H_s norm.
Ω, Γ_f	Continuum and fracture domains
$\Gamma \setminus \Gamma_f$	Boundary domain of the continuum, excluding the fracture domain
$q_n = q_i n_i$	Volume of fluid flowing normal to a surface
q_η	Volume of fluid flowing inwards from the continuum to the fracture domain.

1 Computational framework

2 A high-performance computational framework maximizes computation resources, enables
3 extensive regression tests, and allows for the use of a large number of realizations for uncertainty
4 analyses. This section describes and acknowledges the libraries and tools used to build an
5 automated reproducible design and test environment.

6 The mesh generation engine uses *gmsh* python API (Geuzaine and Remacle, 2009). For this
7 work, the fracture distribution in space is a critical control variable since the objective is to assess
8 the fracture impacts on the effective poroelastic model in a general sense. That means the mesh
9 generation must use mesh recipes on a per-testcase base without user interaction.

10 Conforming fractures are embedded in the domain by *gmsh*. The simulation framework splits
11 the nodes on both sides of each fracture so that the displacement on each side is independent
12 and the fracture mechanics constitutive behavior is assigned between them.

13 The FEM numerical framework is designed in C++ using the open-source libraries *libmesh* (Kirk
14 et al., 2006), PETSc (Balay et al., 2024) and their dependencies as lower-level mathematical
15 implementations.

16 The resulting systems of equations for fully coupled geomechanics are known to be highly ill-
17 conditioned, with conditioning numbers for matrix K ranging up to 10^{12} for drained steps and up
18 to 10^{16} for undrained timesteps (Ferronato et al., 2011; Kardani et al., 2015). A matrix
19 preconditioner is essential during numerical solution. To our experience, the Algebraic Multigrid
20 Implementation *BoomerAMG* preconditioner, available in Hypre library (Henson and Yang, 2002;
21 hypre, n.d.) has shown the most promising results, along with the Bi-Conjugate Gradient
22 Stabilized linear solver available in Petsc (Fokkema, 1996).

23 Test, pre- and post- processing are implemented in *Python* and *GNU make* in an automated and
24 reproducible framework. This framework runs in a light terminal which spawns and control the
25 input and output of the simulator as it runs in an HPC infrastructure.

26 Mesh generation for uncertainty analysis

27 The mesh generator uses the *gmsh*'s Python API to assess the influence of different patterns of
28 fracture distribution on the effective parameters. It defines a 3D uniform grid and randomly

1 assigning N fractures to faces of this grid, such that all fractures are equally sized and normal to
2 an x , y or z axis. Large fractures with different geometries are formed as the density of the
3 fracture increases and the fractures share edges (Fig. 1).

4 Boundary effects are expected when a fracture is partially outside the domain. When an open
5 edge of the fracture crosses the boundary (only part of the fracture is within the domain), one
6 may expect an artificial increase in compliance, which may induce interpretation errors. To avoid
7 that, a test frame is defined, and the numerical domain is built beyond it. This way, all fractures
8 are fully contained in the simulation domain, but some cross the test frame boundary.

9 After conforming mesh generation in *gmsh*, a C++ preprocessor prepares the mesh for usage.
10 The objective is to (1) split the degrees of freedom of the elements touching opposite sides of a
11 fracture, (2) assign necessary boundary condition tags to the element faces, and (3) validate the
12 mesh quality in terms of a number of nodes, elements and element geometry.

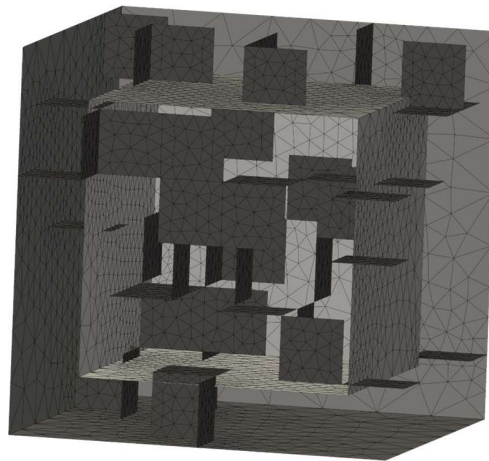


Figure 1 – Example of a mesh with random fractures assigned. The mechanical measurements are done in the internal test frame. The external boundaries are the full domain, intended to minimize boundary effects.

ESTIMATION OF EFFECTIVE PARAMETERS

18 The mechanical description of an effective linear orthotropic poroelastic model comprises four
19 independent parameters. For convenience, the chosen effective parameters are $\bar{\nu}$, \bar{K} , $\bar{\alpha}$, \bar{B} . The
20 three first parameters are *drained* in nature. That is, they are analogous to their counterparts in
21 linear mechanics as no pore pressure variation is observed ($\delta p = 0$). The Skempton coefficient
22 B requires an *undrained* investigation, controlling the mechanical response of the sample to the

pore pressure variation. The permeability κ of the media is assumed to be high enough so that the sample is under a negligible pressure gradient at all times, and the fluid viscosity μ is assumed to be constant (1 cp).

Fig. 2 shows the numerical experiments that provide enough measurements to derive the effective media parameters of the sample. The test case flow is set in 5 steps:

- (a) model initialization with zero displacement and pressure;
- (b) drained isotropic load to determine effective α and K ;
- (c) drained single-side load to determine ν ;
- (d) model reinitialization with zero displacement and pressure;
- (e) undrained isotropic load to determine M .

The boundary displacements are measured as the weighted average of the face displacement. The average pore pressure p and the total variation of fluid content ζ are derived element-by-element, considering both the continuum and the fracture domains. The poroelastic parameters are then determined according to the formulae in Tab. 4 during post-processing of the models.

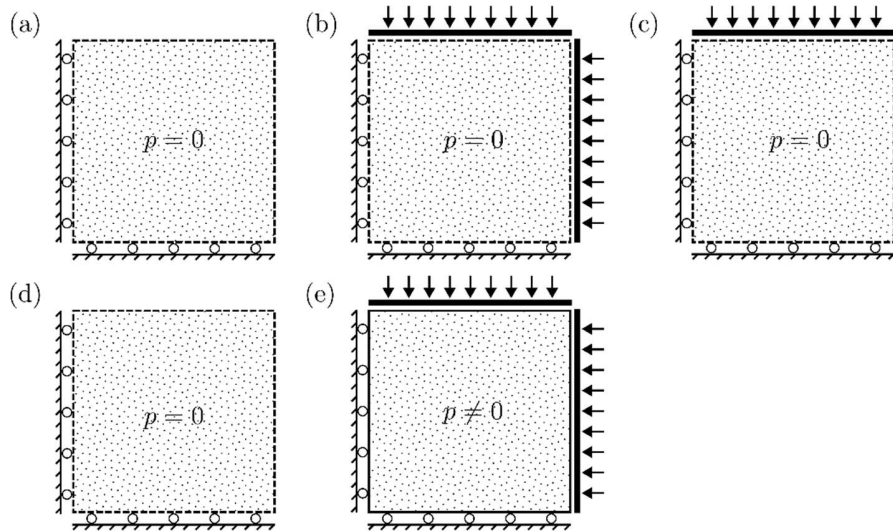


Figure 2 – Step-by-step diagram of the numerical experiment for the estimation of the effective poroelastic parameters. First, drained tests ($p = 0$) estimate K, α and ν (Fig. a-c). Then one undrained test ($p \neq 0$) estimates the Biot Modulus (Fig. d,e). The diagram is in 2D for clarity, experiment is 3D.

1

2

3

Table 4 – Step-by-step computation of the effective poroelastic media parameters after numerical experiment described in Fig 2.

1. Compute volumetric strain	$\epsilon = \frac{\delta V}{V}$
2. Compute effective bulk modulus	$K = \frac{\delta \sigma}{\delta \epsilon} \Big _{\delta p = 0}$
3. Compute fluid content	$\zeta = \frac{\delta V_f}{V}$
4. Compute effective Biot coefficient	$\alpha = \frac{\delta \zeta}{\delta \epsilon} \Big _{\delta p = 0}$
5. Compute effective Poisson ratio	$\nu = - \frac{\delta \epsilon_{yy} + \delta \epsilon_{zz}}{2 \delta \epsilon_{xx}}$
6. Compute effective Skempton coefficient	$B = - \frac{\delta p}{\delta \sigma} \Big _{\delta \zeta = 0}$
7. Compute effective Biot modulus	$M = \frac{1}{S_\epsilon} = \frac{BK}{\alpha(1 - \alpha B)}$

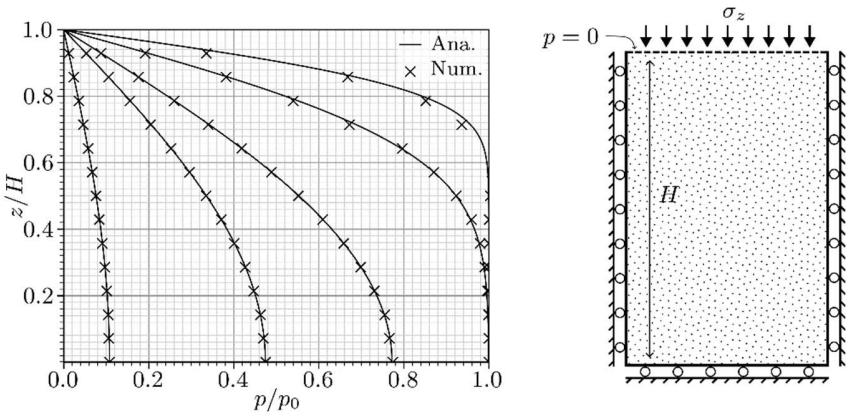
4

5

1 **MODEL VALIDATION**

2 Linear poroelasticity

3 The linear poroelasticity constitutive equation used in the continuum is validated against the
4 analytical solution for Terzaghi's consolidation problem (Von Terzaghi, 1923), as in Fig. 3 and
5 Tab. 5, and against Mandel's problem (Mandel, 1953), as in Fig. 4 and Tab. 6. The model shows
6 satisfactory agreement with the analytical responses, both running in a few seconds to solve
7 systems of up to 2,000 degrees of freedom.



8
9 **Figure 3 – Terzaghi consolidation problem for selected timesteps in good agreement with the**
10 **analytical solution.**

11 **Table 5 – Symbols and parameters for Terzaghi's consolidation test.**

Symbol	Description	Parameter	Value
$t^* = c L^{-2} t$	Adimensional time. In the plot, the shown times are $t^* = \{0.02, 0.05, 0.2, 0.5, 1\}$	G	10^9 Pa
σ_z	Total stress acting normal to the top face of the domain.	M	10^9 Pa
z	Position.	α	0.5
L	Length of the domain.	$\hat{\kappa}$	$10^{-9} \text{ m}^2 \text{ Pa}^{-1} \text{ s}^{-1}$
		ν	0.2

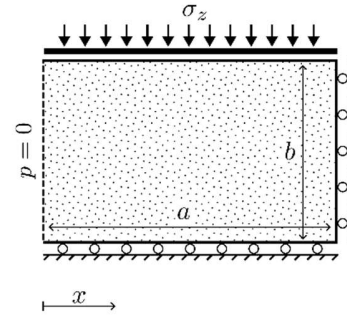
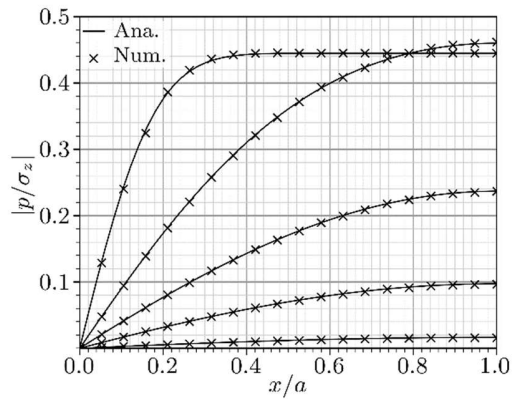


Figure 4 – Mandel's problem for selected timesteps, in good agreement with the analytical solution.

Table 6 – Symbols and parameters for Mandel's problem

Symbol	Description
$t^* = c a^{-2} t$	Adimensional time. In the plot, the shown times are $t^* = \{0.01, 0.1, 0.5, 1, 2\}$
σ_z	Total stress acting normal to the top face of the domain.
x	Position.
a	Domain's half length.
b	Domain's half height.

Parameter	Value
G	10^9 Pa
M	10^{10} Pa
α	1.0
$\hat{\kappa}$	$10^{-10} \text{ m}^2 \text{ Pa}^{-1} \text{ s}^{-1}$
ν	0.2

Fracture specific stiffness

The mechanical behavior of the fractures is described by the normal and shear-specific stiffness, respectively \tilde{E}_η and \tilde{E}_ξ . This test distributes 5 equally spaced fractures and applies stress on the upper side of the domain, as in Fig. 5. The values for stiffness and stress at the boundaries (Tab. 7) were chosen such that a jump of 1 mm is expected across each fracture plane, as is seen in the numerical results.

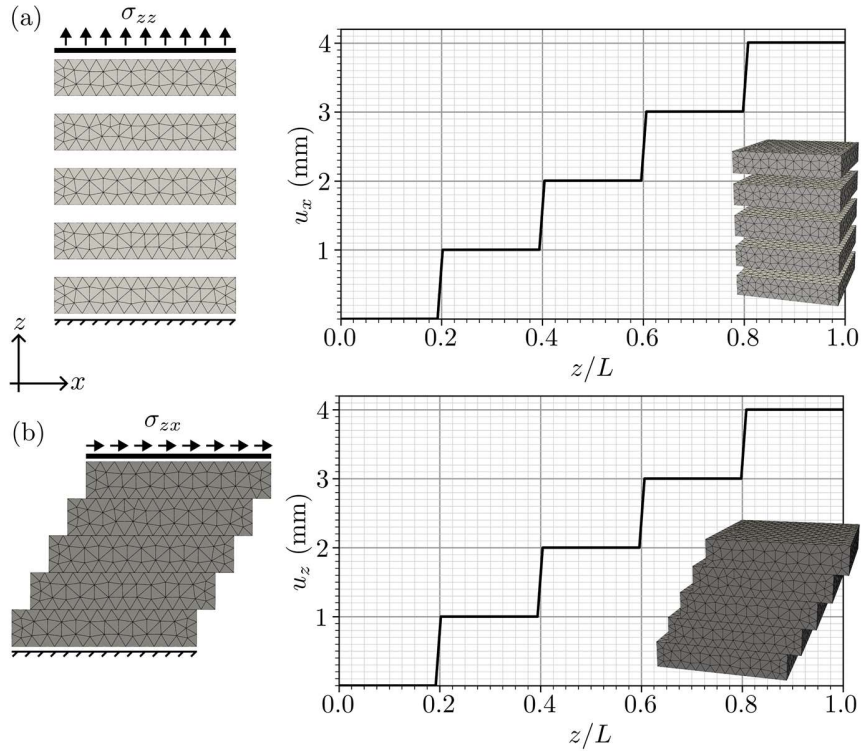


Figure 5 – Validation of the fractures specific stiffness in the (a) normal η and (b) shear ξ directions. The mesh contains 4 fracture planes with linear non-zero stiffness assigned. As numerically $|\sigma_{\square}| = |\tilde{E}_{\square}|$, a jump of 1 m is expected across each fracture plane in the direction of the external stress.

Table 7 – Parameters for the fracture specific stiffness validation.

Parameter	Value
G	$\gg \tilde{E}_{\eta}''$ and $\gg \tilde{E}_{\xi}$
σ_{zz}	10^3 Pa
\tilde{E}_{η}''	10^6 Pa m $^{-1}$
σ_{zx}	10^3 Pa
\tilde{E}_{ξ}	10^6 Pa m $^{-1}$

Sneddon solution

For the validation of the fracture mechanics response to an internal force, a constant pressure is applied along the surface of a circular fracture of radius r in an infinitely wide domain (Fig 6a). The analytic solution for such a problem was proposed by (Sneddon, 1946). Fig 6b shows the accurate match between the numerical and analytical solutions for 5 different fracture radius, using the parameters listed in Tab. 8.

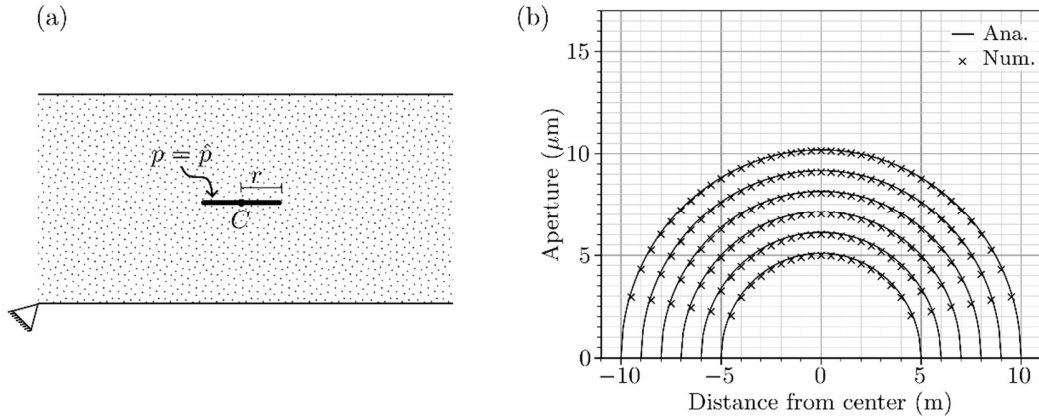


Figure 6 – Validation using Sneddon's solution for a circular fracture located in the center of a large domain, using a constant pressure at the fracture surfaces as the stimulus. (a) Diagram of the boundary conditions for the test. (b) Comparison of the analytical and numerical solutions for 5 different fracture radius {5, 6, 7, 8, 9} m. The maximum observed relative error was 1.9%.

Table 8 – Parameters for the Sneddon validation test.

Parameter	Value
\hat{p}	10^3 Pa
G	10^9 Pa
ν	0.2
α	0

Mass balance of an open fracture

This validation test ensures that the overall fluid volume in the domain remains constant after running an undrained timestep so that the volume of fluid filling the fracture is equal to the volume drained from the continuum. The variation of the fluid volume in the continuum is calculated on an element-by-element basis as

$$\delta V_{matrix} = \int_{\Omega} \zeta \, d\Omega = \int_{\Omega} (\alpha \epsilon + p \, S_{\epsilon}) \, d\Omega \quad . \quad (30)$$

The fracture volume is calculated by direct integration of the volume along the fracture surfaces as

$$\delta V_{fracture} = \int_{\Gamma_f} w_{\eta} \, d\Gamma_f \quad , \quad (31)$$

where w_{η} is the normal aperture of the fracture at a point. Considering the fluid density to be constant, the relative mass balance error is approximated by

$$V_{err} = \frac{\delta V_{fracture} - \delta V_{matrix}}{\delta V_{fracture}}$$

For this validation, 5000 realizations were tested, in a Monte Carlo setup, as described in Tab. 9. Fig. 7b shows the resulting error distribution. The expected relative absolute error is in the order of 10^{-4} , with 90% of the realizations below 8.6×10^{-4} . Such error magnitudes were considered acceptable to the tested scenarios.

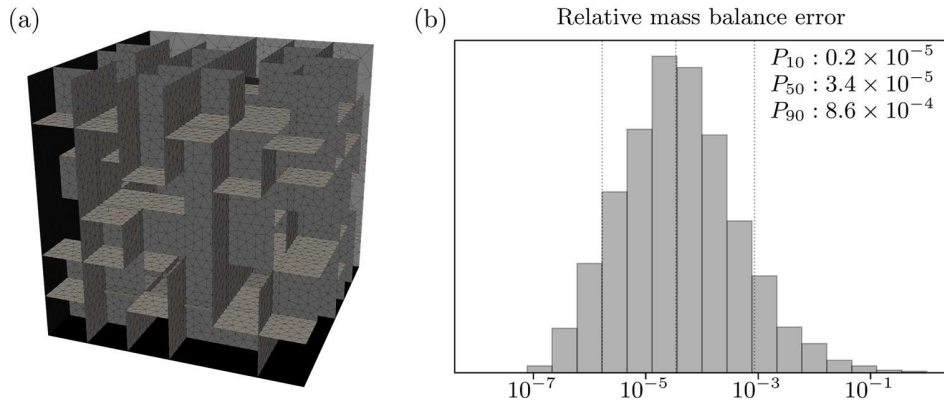


Figure 7 – Validation of the volume balance of different sets of fractures. (a) A sample mesh with a random set of fractures assigned. (b) The histogram shows results for 5000 tests with varied fracture density and matrix parameters, as well as important quantiles (P_{10} , P_{50} , P_{90}). A relative error below 10^{-3} is expected in the volume balance.

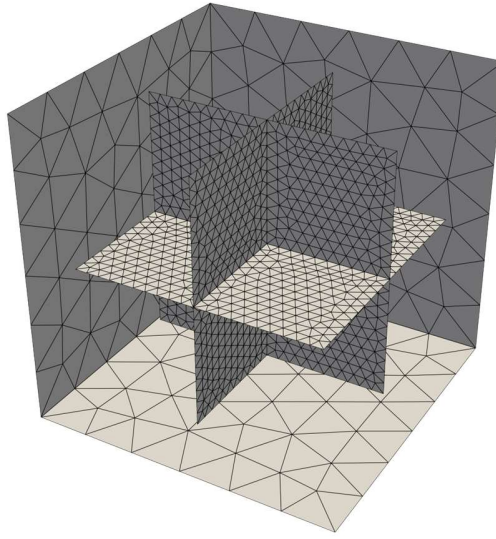
Table 9 – Statistical distribution of the input parameters for the Monte Carlo simulations targeting mass balance validation

Symbol	
N	5000
K	$10^8 - 10^{10}$ Pa
α	0.2 – 0.8
B	0 – 1
ν	0.2 – 0.45
\tilde{E}_η	$10^4 - 10^8$ Pa m ⁻¹
\tilde{E}_ξ	10^{12} Pa m ⁻¹
Frac density	0 – 0.28

1 RESULTS

2 Sensitivity to matrix and fracture attributes

3 This application focuses on understanding the overall sensitivity of the effective parameters to
4 the matrix and fracture-specific stiffness attributes. For that, an orthotropic system with a fixed
5 single set of fractures is meshed, as in Fig. 8.



6
7 **Figure 8 – Orthotropic testcase, with three planes of fractures added.**

8 The key parameter is the specific stiffness of the fracture. For that, three base cases are defined:
9 (1) very low specific stiffness ($\tilde{E}_\eta = \tilde{E}_\xi = 10^4$ Pa), where the fractures are totally open and
10 practically cohesion-free, (2) average specific stiffness ($\tilde{E}_\eta = \tilde{E}_\xi = 10^8$), where the fracture
11 cohesion offers partial elastic resistance to strain, and (3) high specific stiffness ($\tilde{E}_\eta = \tilde{E}_\xi =$
12 10^{12} Pa), where the fractures are mechanically invisible, and the matrix constitutive model
13 dominates. From the three base cases, several different set of parameters are derived. Fig. 9
14 and 10 show the correlations observed after inspection of 543 different scenarios.

15 Fig. 8 shows the impact of the fractures in all four effective parameters observed, with a smooth
16 transition as the fracture stiffness drops from high to low stiffness. The solid dots pinpoint the
17 reference cases mentioned earlier. While the effective bulk modulus \bar{K} drops approximately
18 50%, The influence of the fracture on the other parameters is remarkable. In such a simple
19 experiment, the effective model is highly sensitive to open fractures.

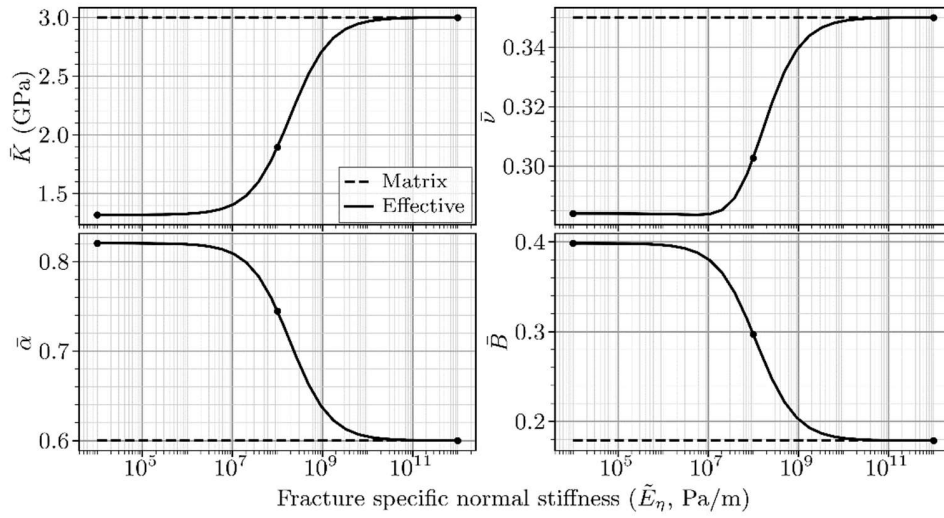


Figure 9 – Effective parameters sensitivity to the fracture specific normal stiffness.

The plot tile in Fig. 10 show the effective model's response to different matrix attributes. The horizontal axes represent a span of each poroelastic matrix parameter, and the vertical axes represent the relative variation of each effective parameter, having its matrix counterpart as reference. The high stiffness case (solid line) is a control case, where the fractures are mechanically transparent, and the results are expected to be unitary.

As is clear from the figure, \bar{K} and $\bar{\nu}$ relative decrease depends only on its matrix counterparts. Their effective values are independent of the matrix attributes α and M . The effective poroelastic $\bar{\alpha}$ and \bar{B} show a high increase for low α , meaning that it is unlikely to observe low values for those parameters in NFRs near a tensile regime. The Biot modulus \bar{M} , which is inversely related to the storage capacity under constant strain, decreases significantly as the ratio M/K increases. That is, the less compressive the pore space and fluid (higher M), the more significant is the fluid storage added (or removed) by the opening (or closing) fractures.

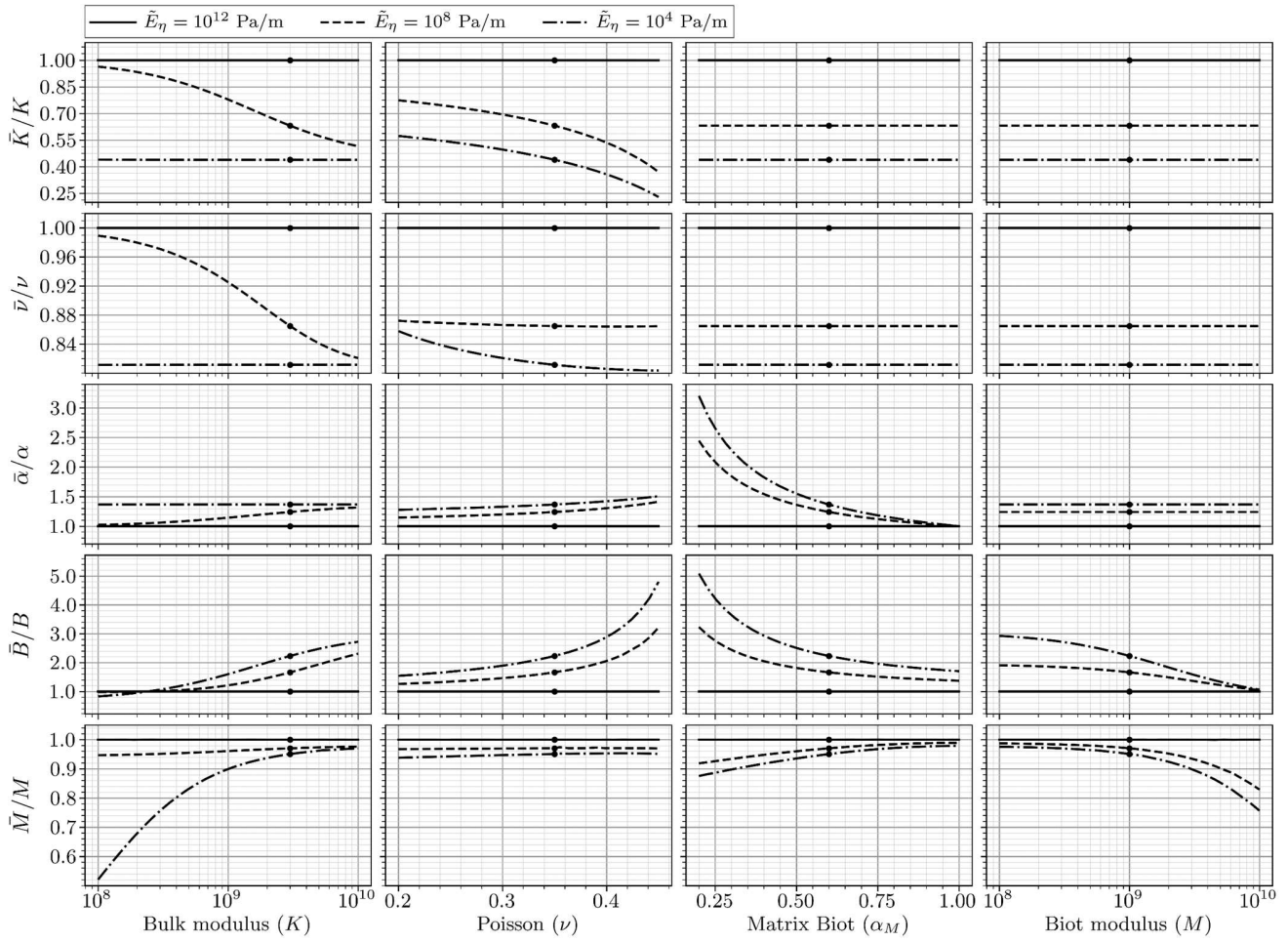


Figure 10 – Sensitivity of the effective parameters to different matrix parameters considering three different fracture specific stiffness, E_η : 10^4 (low cohesion), 10^8 (moderate cohesion) and 10^{12} (total cohesion).

Table 10 – Symbols for the symmetric orthotropic test

Symbol	Reference cases	Ranges
N	543	–
K	3×10^9 Pa	$10^8 - 10^{10}$ Pa
α	0.6	0.2 – 1
M	10^9 Pa	$10^8 - 10^{10}$ Pa
ν	0.35	0.2 – 0.45
$\tilde{E}_\eta = \tilde{E}_\xi$	$\{10^4, 10^8, 10^{12}\}$ Pa	$10^4 - 10^{12}$ Pa/m
L	50 m	50 m
Fracture length	30 m	30 m

Sensitivity to fracture density

This section discusses the impact of the fracture intensity on the effective poroelastic model. The 3D fracture intensity parameter p_{32} is defined as the fracture surface S_f per unit of rock volume (Dershowitz and Herda, 1992), that is

$$p_{32} = \frac{S_f}{V} . \quad (32)$$

Given the definition of the domain boundary and the number of fractures, the mesh is generated automatically. The matrix poroelastic parameters are constant in every realization, so the fracture density is the only parameter to vary. The fractures are assumed to be open, with negligible cohesion.

The results show consistent correlations between p_{32} and the effective parameters (Fig. 11). Although the randomness is limited to an orthogonal grid due to the mesh generation technique, the trends are clear, showing a one-order reduction in \bar{K} , a three-fold reduction in $\bar{\nu}$ and \bar{B} and $\bar{\alpha}$ converging to 1 as the fracture density increases. As the fracture intensity of NFRs can be significantly higher than the range tested, the best parameters to input in such cases may be simply the extrapolation of the parameters shown here.

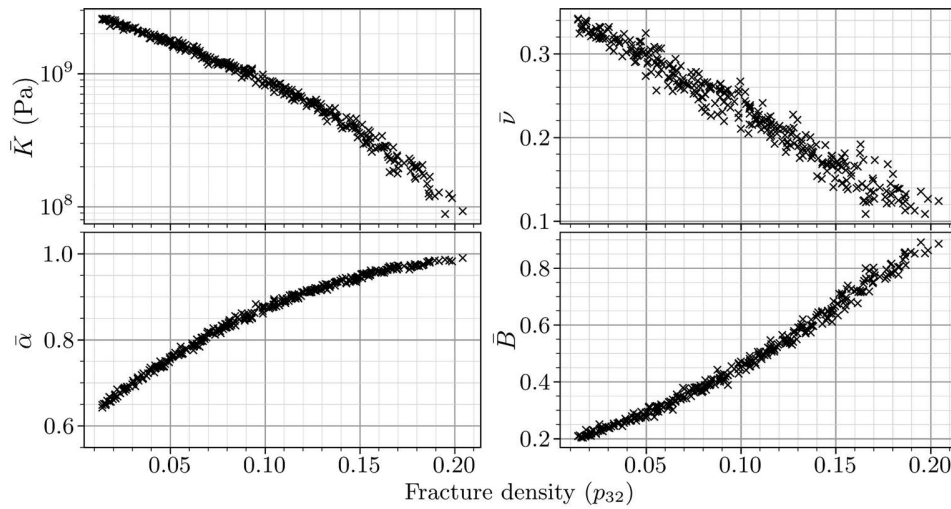


Figure 11 – Sensitivity to fracture density (p_{32}).

1

Table 11 – Symbols for the fracture density test

Symbol	
N	320
K	2.7 GPa
ν	0.35
α	0.6
B	0.178
M	10^9 Pa
$\tilde{E}_\eta = \tilde{E}_\xi$	10^4 Pa m ⁻¹
N_{frac}	25 – 500
p_{32}	0.01 – 0.21
Fracture spacing	11.67 m
Side of the domain	70 m
Side of the test frame	50 m

2

3 Sensitivity to the fluid compressibility

4 This section aims to assess the influence of fluid compressibility on the effective poroelastic
5 model. The parameters typical of a naturally fractured consolidated carbonate rock were used
6 for the matrix poroelasticity (Morschbacher et al., 2024). The fracture distribution was built after
7 the mesh generator previously discussed. Five different fluids of interest were characterized:
8 Methane, Carbon Dioxide, Hydrogen, Oil and Water (Peter J. Linstrom and Mallard, 2001). Tab.
9 12 lists the complete set of parameters used for the test case.

10 Fig. 12 shows clearly the independence of the poroelastic effective drained parameters \bar{K} , $\bar{\alpha}$ and
11 $\bar{\nu}$ to the fluid compressibility. The effective parameters transition smoothly from their matrix
12 counterparts (high \tilde{E}_η) to the cohesive free scenario (low \tilde{E}_η) and the curves for all the fluids
13 overlap.

14 Fig. 13 shows the impact of the fluid on the undrained parameters \bar{M} and \bar{B} , where the distinct
15 response is seen for each fluid. Consistently, the fracture storage at constant strain increases
16 (lower M) for less compressible fluids (water and oil) as the fracture cohesion decreases. When
17 more compressible fluids are assessed, the matrix concentrates the fluid storage, and the
18 mechanical fracture aperture is irrelevant to the effective response.

19 From the Skempton coefficient perspective, a significant increase is seen as the fracture
20 cohesion reduces. This is expected as the fluid that occupies the fracture voids interacts with
21 the fracture surfaces. In an environment of low compressibility, the boundary stresses propagate

- 1 seamlessly to the fracture network, compressing (or expanding) the fluid integrally. In the limit,
- 2 $\bar{B} \rightarrow 1$.

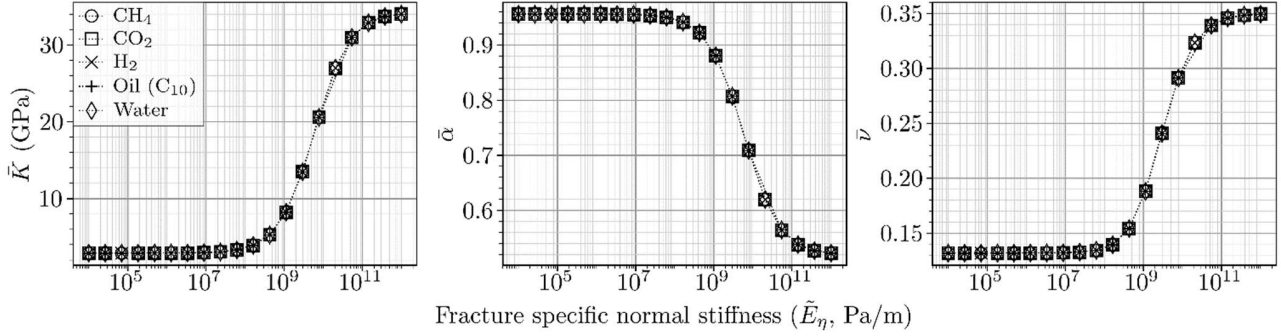


Figure 12 – Testcase considering multiple fractures distributed – volumetric parameters.

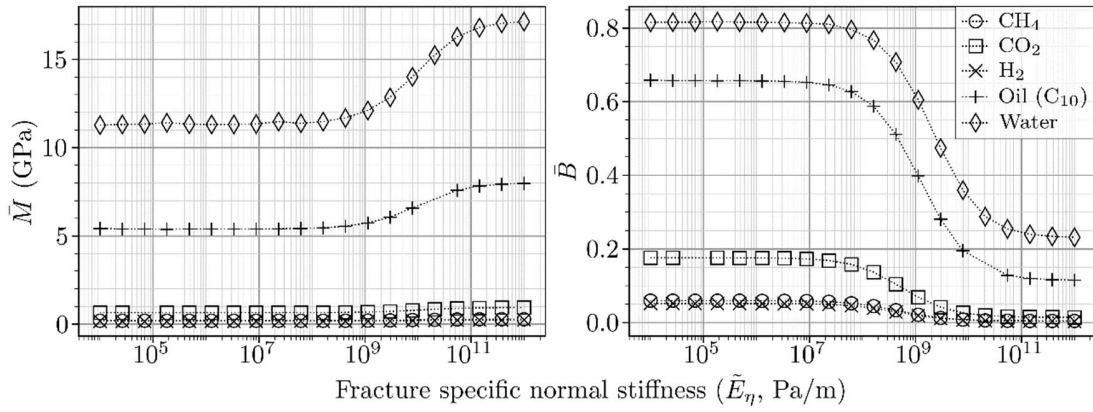


Figure 13 – Testcase considering multiple fractures distributed – undrained parameters.

Table 12 – Symbols for the fluid sensitivity test

Symbol	Value
N	100
K	$34.1 \times 10^9 \text{ Pa m}^{-1}$
α	0.52
ν	0.35
$\tilde{E}_\eta = \tilde{E}_\xi$	10^4 Pa m^{-1}
p_{32}	0.17
K_s	70 GPa

Symbol	Value
ϕ	13%
T	60°C
P	20 MPa
Fracture spacing	11.67 m
Domain side	70 m
Test frame side	50 m

Fluid bulk modulus at P and T	
$K_{f\text{H}_2}$	0,0315 GPa
$K_{f\text{CH}_4}$	0,0365 GPa
$K_{f\text{CO}_2}$	0,123 GPa
$K_{f\text{C}_{10}}$	1,09 GPa
$K_{f\text{Wat}}$	2,49 GPa

Biot modulus at P and T	
M_{H_2}	0.24 GPa
M_{CH_4}	0.280 GPa
M_{CO_2}	0.941 GPa
$M_{\text{C}_{10}}$	8 GPa
M_{Wat}	17.2 GPa

1

2 Uncertainty assessment

3 The previous sections assessed the impact of individual parameters on the effective response
4 of the medium. Now, recognizing that the parameters are uncertain and interrelated, the
5 objective is to build a posteriori distributions for each poroelastic parameter. In other words, the
6 idea is to find rules of thumb for designers building geomechanical models for NFRs.

7 A Monte Carlo simulation setup was built considering uniform (linear or logarithmic) distributions
8 for the matrix properties (Tab. 13). This is the equivalent of assuming a known range for each
9 property, but there is no better guess inside this range. Such a setup can guide how a random
10 set of fractures would impact such uniform distributions.

11 Fig. 14 shows the results. The first column shows the *a priori* distributions for each parameter.
12 The second column shows the *a posteriori* distribution (the effective assessment of each
13 parameter after the fractures are considered). The rightmost column scatters the realizations:
14 the horizontal axes represent the matrix property, and the vertical axes represent the resulting
15 effective property.

16 It is clear that the distributions of the effective parameters (second column) are not uniform
17 anymore after the fractures are considered. Moreover, although the uncertainty is still high, each
18 parameter follows a specific trend:

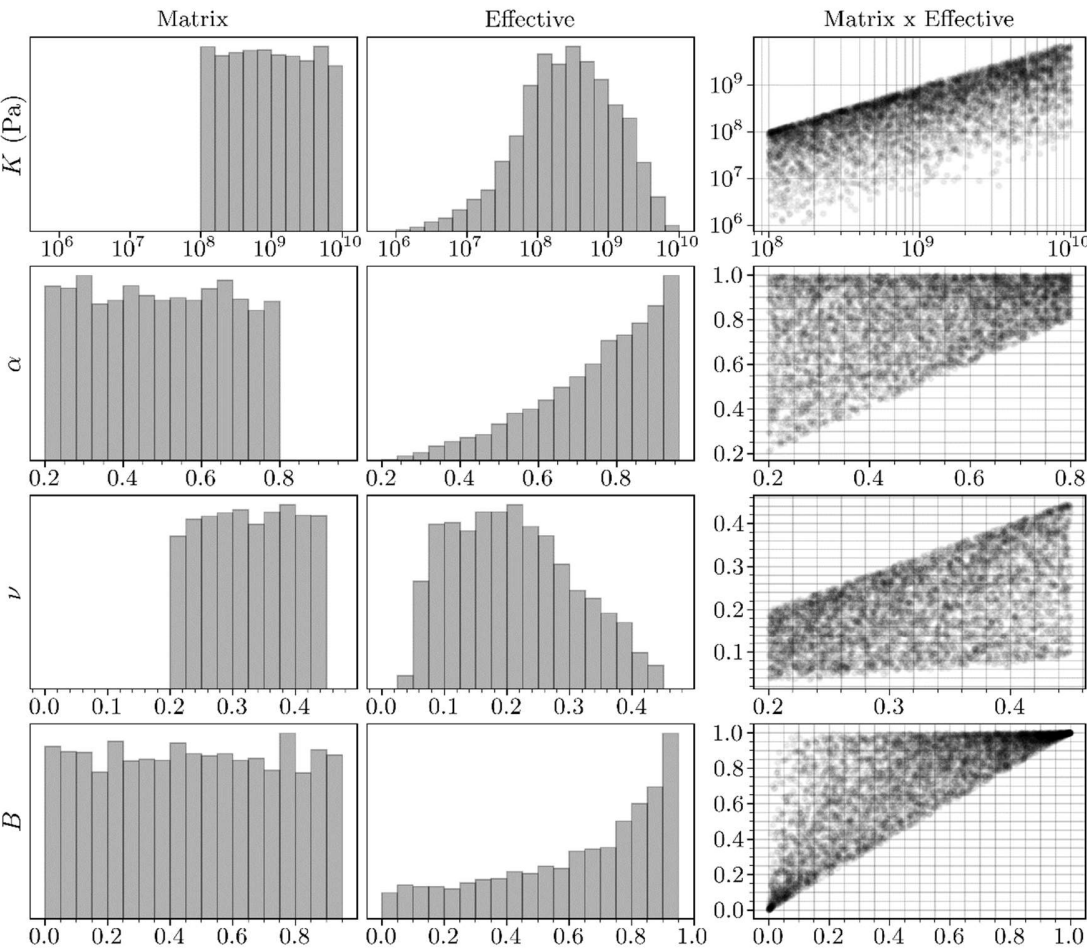
19 (a) \bar{K} tends to lower by almost 10-fold in average (the effective media is more compliant).
20 High values are filtered out by the fractures, and realizations up to 1000-fold lower \bar{K} are
21 observed.

22 (b) $\bar{\alpha}$ tends to 1, with very small-valued realizations being filtered out.

23 (c) $\bar{\nu}$ reduces significantly, showing an average of less than half the original. This means that
24 the fractures reduce the axial stresses from the transversal strain of the effective REV.
25 We note that these results are likely biased by the mesh generation strategies and by the
26 assumption that the fracture specific stiffness tensor is diagonally dominant. Higher $\bar{\nu}$
27 would likely emerge in cases with inclined or rough fractures..

28 (d) \bar{B} tends to 1 as the fractures tend to add a stronger interaction between the stresses and

1 the porous pressure.



2
3 **Figure 14 – A priori and a posteriori distribution of parameters showing the effect of a set of**
4 **random fractures in the expected effective parameters. Each point in the plots on the right**
5 **shows a realization of the monte carlo simulation, qualitatively showing the behavior of each**
6 **effective parameter compared to the unfractured one.**

7 **Table 13 – Symbols for the fluid sensitivity test**

Symbol	Value
N	5000
K	$10^8 - 10^{10}$ (logarithmic)
α	0.2 – 0.8 (uniform)
ν	0.2 – 0.45 (uniform)
B	0 – 1 (uniform)
\tilde{E}_η	$10^4 - 10^9$ (logarithmic)
\tilde{E}_ξ	10^{12}
Fracture spacing	11.67 m
Domain side	70 m
Test frame side	50 m

1

2 CONCLUSIONS

3 This paper introduced a high-performance poroelastic simulator dealing with conforming fracture
4 domains explicitly added to the mesh, as well as its formulation and validation procedures. The
5 results provide geomechanical analysts with insights into the impact of fractures in the large-
6 scale response of fractured rock masses. Our approach contrasts with the literature, as the
7 poroelastic parameters are considered simultaneously. Results showed the significant impact of
8 even sparse fracture networks in large-scale behavior.

9 The sensitivity of the effective model to the presence of joints was remarkable, even when a low-
10 density fracture network was considered. Such observation must be considered when dealing
11 with reservoirs subject to low effective pressure, as is the case of shallow formations, highly
12 pressurized systems, or rocks with lower temperatures due to cold fluid injection. In high-
13 effective pressure environments, the fractures tend to be mechanically transparent as their
14 specific stiffness increase.

15 For the cases tested, fracture density (p_{32}) could predict the impact of the fractures in the
16 effective model. As p_{32} increases, the effective media becomes more compliant (lower bulk
17 modulus), the effective Biot modulus increases towards 1, and Skempton coefficient also
18 increases towards 1. Considering simplistic fracture domain constitutive models and geometries,
19 a dense fracture network tends to decouple axial stress and normal strains (lower Poisson
20 coefficient). However, this behavior may differ in cases where inclined fracture planes and
21 surface roughness are considered. In such scenarios, axial stresses may act in the direction of
22 fracture slip with associated transversal strains.

23 The REV fluid storage capacity was sensitive to the presence of fractures for lower
24 compressibility fluids. On the other hand, the rock matrix dominates fluid storage for
25 compressible gases, and insignificant variation was found in the presence of fractures.

26 Similar to fluid flow modeling, properties must be upscaled from lab-scale tests into effective
27 field-scale counterparts. Acknowledging the interdependence among the poroelastic
28 parameters, Monte Carlo simulations provided rules-of-thumb for model design in the presence
29 of uncertain fracture networks. This work illustrates such a workflow and how the uncertainty

1 would change from uniform to a more realistic distribution.

2 The ideas discussed herein foster the discussion of mechanical upscaling in the presence of
3 fractures and joints. The non-linear transient thermos-hydro-mechanical response of rocks,
4 especially near injectors, still lacks investigation. Designers must consider the multi-physics
5 environment and avoid oversimplifying.

6 We observe reservoir rock compliance increases in higher pressure and when lower temperature
7 is induced, usually implying higher stress contrast to the caprock near injection wells. Moreover,
8 in cases where the fluid compressibility is high, the poroelastic effective media reduces to a
9 drained response, and incorporating the effective behavior in geomechanical models becomes
10 trivial. The results suggest that using effective parameters favors safety and tends to improve
11 the economic returns of EOR, CCS, and Hydrogen storage projects.

12

REFERENCES

- Aguilera, R., 1998. Geologic aspects of naturally fractured reservoirs. *The Leading Edge* 17, 1667–1670.
- Balay, S., Abhyankar, S., Adams, Mark.F., Benson, S., Brown, J., Brune, P., Buschelman, K., Constantinescu, Emil, M., Dalcin, L., Dener, A., Eijkhout, V., Faibussowitsch, J., Gropp, W.D., Hapla, V., Isaac, T., Jolivet, P., Karpeev, D., Kaushik, D., Knepley, M.G., Kong, F., Kruger, S., May, D.A., McInnes, L.C., Mills, R.T., Mitchell, L., Munson, T., Roman, J.E., Rupp, K., Sanan, P., Sarich, J., Smith, B.F., Zampini, S., Zhang, H., Zhang, J., 2024. PETSc Web page.
- Bandis, S.C., Lumsden, A.C., Barton, N., 1983. Fundamentals of rock joint deformation. *International Journal of Rock Mechanics and Mining Sciences & Geomechanics Abstracts* 20, 249–268.
- Barton, N., Bandis, S., 1982. Effects of block size on the shear behavior of jointed rock, in: *ARMA US Rock Mechanics/Geomechanics Symposium*. Berkeley, CA, pp. 739–760. <https://doi.org/10.2307/jj.9669308.78>
- Biot, M.A., 1941. General theory of three-dimensional consolidation. *J Appl Phys* 12, 155–164.
- Boutéca, M., Guéguen, Y., 1999. *Mechanical Properties of Rocks: Pore Pressure and Scale Effects*, Oil & Gas Science and Technology-Rev. IFP.
- Brace, W.F., Martin, R.J., 1968. A test of the law of effective stress for crystalline rocks of low porosity. *International Journal of Rock Mechanics and Mining Sciences* 5, 415–426. [https://doi.org/10.1016/0148-9062\(68\)90045-4](https://doi.org/10.1016/0148-9062(68)90045-4)
- Chen, S., Zhao, Z., Chen, Y., Yang, Q., 2020. On the effective stress coefficient of saturated fractured rocks. *Comput Geotech* 123. <https://doi.org/10.1016/j.compgeo.2020.103564>
- Cheng, A.H.-D., 2016. *Poroelasticity*. Springer International Publishing, Switzerland. <https://doi.org/10.1007/978-3-319-25202-5>
- Cornet, F.H., Fairhurst, C., 1974. Influence of Pore Pressure on the Deformation Behavior of Saturated Rocks, in: *Proc. 3rd Congress ISRM*. National Academy of Sciences, Denver, pp. 638–644.

1 Cundall, P.A., 1971. A computer model for simulating progressive large-scale movements in
2 blocky rock systems. *Rock fracture: proceedings of the International Symposium on Rock*
3 *Mechanics*. 1, 129–136.

4 De Simone, S., Darcel, C., Kasani, H.A., Mas Ivars, D., Davy, P., 2023. Equivalent Biot and
5 Skempton Poroelastic Coefficients for a Fractured Rock Mass from a DFN Approach. *Rock*
6 *Mech Rock Eng* 56, 8907–8925. <https://doi.org/10.1007/s00603-023-03515-9>

7 Dershowitz, W.S., Herda, H.H., 1992. Interpretation of fracture spacing and intensity, in: *ARMA*
8 *US Rock Mechanics/Geomechanics Symposium*.

9 Ferronato, M., Janna, C., Pini, G., 2011. Parallel solution to ill-conditioned FE geomechanical
10 problems. *Int J Numer Anal Methods Geomech* 422–437. <https://doi.org/10.1002/nag>

11 Fokkema, Diederik.R., 1996. Enhanced Implementation of BiCGstab (l) for Solving Linear
12 Systems of Equations.

13 Geuzaine, C., Remacle, J., 2009. Gmsh: A 3-D finite element mesh generator with built-in pre-
14 and post-processing facilities. *Int J Numer Methods Eng* 79, 1309–1331.

15 Ghaboussi, J., Wilson, E.L., Isenberg, J., 1973. Finite element for rock joints and interfaces.
16 *Journal of the soil mechanics and foundations division* 99, 833–848.

17 Goodman, R.E., Taylor, R.L., Brekke, T.L., 1968. A model for the mechanics of jointed rock.
18 *Journal of the soil mechanics and foundations division* 94, 637–659.

19 Grechka, V., Kachanov, M., 2006. Effective elasticity of fractured rocks: A snapshot of the work
20 in progress. *Geophysics* 71. <https://doi.org/10.1190/1.2360212>

21 Guéguen, Y., Kachanov, M., 2011. Effective elastic properties of cracked rocks - An overview.
22 *Mechanics of crustal rocks* 73–125.

23 Henson, V.E., Yang, U.M., 2002. BoomerAMG: A parallel algebraic multigrid solver and
24 preconditioner. *Applied Numerical Mathematics* 41, 155–177.
25 [https://doi.org/10.1016/S0168-9274\(01\)00115-5](https://doi.org/10.1016/S0168-9274(01)00115-5)

26 Hughes, T.J.R., 2000. *The finite element method: linear static and dynamic finite element*
27 *analysis*, Reprint. ed. Dover Publications, Inc.

28 hypre: High Performance Preconditioners [WWW Document], n.d. URL

1 <https://lnl.gov/casc/hypre>

2 Kardani, O., Lyamin, A. V, Krabbenhøft, K., 2015. Parallel preconditioned conjugate gradient
3 method for large sparse and highly ill-conditioned systems arising in computational
4 geomechanics 11.

5 Kirk, B.S., Peterson, J.W., Stogner, R.H., Carey, G.F., 2006. libMesh : a C++ library for parallel
6 adaptive mesh refinement/coarsening simulations. Eng Comput 22, 237–254.
7 <https://doi.org/10.1007/s00366-006-0049-3>

8 Lomize, G.M., 1951. Water flow through jointed rock (in Russian).

9 Long, J.C.S., Remer, J.S., Wilson, C.R., Witherspoon, P.A., 1982. Porous media equivalents for
10 networks of discontinuous fractures. Water Resour Res 18, 645–658.

11 Mandel, J., 1953. Consolidation des sols (étude mathématique) (Consolidation of soils
12 (mathematical study))). Geotechnique 3, 287–299.

13 Marinelli, F., Van Den Eijnden, A.P., Sieffert, Y., Chambon, R., Collin, F., 2016. Modeling of
14 granular solids with computational homogenization: Comparison with Biot’s theory. Finite
15 Elements in Analysis and Design 119, 45–62. <https://doi.org/10.1016/j.finel.2016.05.003>

16 Min, K.B., Jing, L., 2003. Numerical determination of the equivalent elastic compliance tensor
17 for fractured rock masses using the distinct element method. International Journal of Rock
18 Mechanics and Mining Sciences 40, 795–816. [https://doi.org/10.1016/S1365-
19 1609\(03\)00038-8](https://doi.org/10.1016/S1365-1609(03)00038-8)

20 Morschbacher, M.J., Fernandes Vasquez, G., Figueiredo, M.P., Cesar, J., Justen, R., De
21 Oliveira, F., Falcao, L., Lucia, A., Maria, M., 2024. Biot Coefficient From Sonic Logs With
22 Laboratory Data Calibration: a Brazilian Pre-Salt Field Case Study.
23 <https://doi.org/10.30632/SPWLA-2024-0003>

24 Murad, M.A., Loula, A.F.D., 1994. On Stability and Convergence of Finite Element
25 Approximations of Biot’s Consolidation problem. Int J Numer Methods Eng 37, 645–667.

26 Narr, W., Schechter, D.S., Thompson, L.B., 2006. Naturally fractured reservoir characterization.
27 Society of Petroleum Engineers Richardson, TX.

28 Nelson, R.A., 2001. Geologic analysis of naturally fractured reservoirs. Gulf Professional

Publishing.

Oda, M., 1986. An equivalent continuum model for coupled stress and fluid flow analysis in jointed rock masses. *Water Resour Res* 22, 1845–1856.

Peter J. Linstrom, Mallard, W.G., 2001. The NIST Chemistry WebBook: A Chemical Data Resource on the Internet [WWW Document]. URL (accessed 8.25.24).

Poli, R., Gioria, R., Carrion, R., 2021. A poroelastic simulator with hydraulic fracture propagation using cohesive finite elements. *Journal of the Brazilian Society of Mechanical Sciences and Engineering* 43, 1–13. <https://doi.org/10.1007/s40430-020-02787-4>

Pyrak-Nolte, L.J., Morris, J.P., 2000. Single fractures under normal stress: The relation between fracture specific stiffness and fluid flow. *International Journal of Rock Mechanics and Mining Sciences* 37, 245–262. [https://doi.org/10.1016/S1365-1609\(99\)00104-5](https://doi.org/10.1016/S1365-1609(99)00104-5)

Rice, J.R., 1977. Pore Pressure Effects in Inelastic Constitutive Formulations for Fissured Rock Masses. *Advances in Civil Engineering Through Engineering Mechanics* 295–297.

Sneddon, I.N., 1946. The distribution of stress in the neighbourhood of a flat elliptical crack in an elastic solid. *Proc. Roy. Soc.A* 187, 229–260. <https://doi.org/10.1098/rspa.1946.0077>

Von Terzaghi, K., 1923. Die Berechnung der Durchlässigkeitsziffer des Tones aus dem Verlauf der hydrodynamischen Spannungserscheinungen (A method of calculating the permeability of clay from the history of hydrodynamic stress variation). *Mathematisch-Naturwissenschaftliche Klasse* 132, 125–138.

Wang, H.F., 2000. Theory of linear poroelasticity with applications to geomechanics and hydrogeology. Princeton University Press, Princeton, Estados Unidos.

Witherspoon, P.A., Wang, J.S.Y., Iwai, K., Gale, J.E., 1980. Validity of cubic law for fluid flow in a deformable rock fracture. *Water Resour Res* 16, 1016–1024.

Zareidarmiyan, A., Parisio, F., Makhnenko, R.Y., Salarirad, H., Vilarrasa, V., 2021. How Equivalent Are Equivalent Porous Media? *Geophys Res Lett* 48, 1–11. <https://doi.org/10.1029/2020GL089163>